Microstructure and tribological behaviors of FeCoCrNiMoSi$_x$ high-entropy alloy coatings prepared by laser cladding

Yucheng Yang [a, 1], Yaojia Ren [a, 1], Yanwen Tian [a], Kaiyang Li [b], Lichun Bai [c], Qianli Huang [a, ***], Quan Shan [d, **], Yingtao Tian [e], Hong Wu [a, *]

[a] *State Key Laboratory of Powder Metallurgy, Central South University, Changsha 410083, P.R. China;*

[b] *Department of Chemical and Materials Engineering, University of Alberta, Edmonton, Alberta, T6G 1H9, Canada;*

[c] *Key Laboratory of Traffic Safety on Track (Central South University), Ministry of Education, School of Traffic & Transportation Engineering, Central South University, Changsha, 410075, P.R. China;*

[d] *Academy of Materials Science and Engineering, Kunming University of Science and Technology, Kunming, P.R. China;*

[e] *Department of Engineering, Lancaster University, Bailrigg, Lancaster LA1 4YW, United Kingdom.*

[*] *Corresponding author.*

[**] *Corresponding author.*

[***] *Corresponding author.*

[1] *These authors contributed equally to this work.*

E-mail address:

hwucsu@csu.edu.cn; wuhong927@126.com (Hong Wu),

quanshan.ms@gmail.com (Quan Shan),

hql1990@163.com (Qianli Huang).

Abstract: FeCoCrNiMo high-entropy alloy (HEA) has attracted great interests due to its excellent corrosion resistance, but it suffers relatively low hardness and poor tribological performance. In this work, a systematic study on microstructural evolution and tribological behavior of equiatomic $FeCoCrNiMoSi_x$ (x = 0.5, 1.0, 1.5) HEA coatings prepared by laser cladding (LC) on Q235 steel substrates is reported. Confirmed by X-ray diffraction analysis (XRD) and energy dispersive spectrometry (EDS) results, these coatings mainly consist of Fe-rich FCC and FeMoSi phases. The increase of Si content leads to greater lattice distortion and promotes the formation of Si-rich intermetallics, which can significantly improve the hardness and the wear resistance of the $FeCoCrNiMoSi_x$ coatings. The best wear resistance is achieved in $FeCoCrNiMoSi_{1.0}$ coating, where the wear mechanism is a combined abrasive and adhesive wear.

1. Introduction

Recently, high-entropy alloys (HEAs) have received increasing interests due to the enormous possibilities in finding new composition, which can potentially form novel microstructure and provid exceptional properties [1-4]. HEAs are defined as alloys consisted of five or more principal alloying elements with atomic weighting randing between 5-35% [5, 6], which generally exhibit simple solid solution phase as FCC, BCC or HCP crystal structure due to their high entropy of mixing [7, 8].

Many researchers have devoted themselves to the study of high hardness and great tribological properties of HEAs for years. Li et al. [9] successfully manufactured a FeCoCuAlNi HEA coating, which presented a super-high hardness of 15.4 GPa and an elasticity of 161 GPa. Zhang et al. [10] fabricated the TiZrNbWMo refractory HEA coating on the surface of 45# steel and obtained a microhardness of 700 HV in the as-built coating, which was three times of the 45# steel due to the formation of β-Ti_xW_{1-x} precipitates. Wang et al. [11] reported that a $MoFe_{1.5}CrTiWAlNb$ HEA coating was fabricated on M2 tool steel, which exhibited a maximal hardness of 910 HV and great wear resistance with abrasive wear mechanism. Cai et al. [12] successfully introduced a remelted NiCrCoTiV HEA coating possessing a higher friction coefficient and lower wear mass loss compared with the as-built HEA coating.

As a popular HEA, FeCoCrNiMo has been investigated by many researchers due to its excellent corrosion resistance [13-15]. However, the relatively low hardness (maximal value of 500 HV) and poor tribological behaviors at room temperature restrict its further applications in the aerospace and automobile industries [16-18]. Silicon, as

a widely available and cost-effective strengthening element, has been often employed to improve the performance of HEAs for years. The increase of Si promoted the formation of BCC phase in AlCoCrCuFeNi system, which provided better mechanical properties for AlCoCrCuFeNi HEA [19]. In the AlCoCrFeNi system, the addition of Si improved the hardness owing to inducing the precipitation of Cr_3Si intermetallics [20]. In another study carried out by Gorr et al. [21], the addition of silicon in AlCoCrNiMoFeSi led to the formation of FeMoSi phase, which significantly improved the tribological properties of the alloys.

In this study, a number of $FeCoCrNiMoSi_x$ HEA with different Si addition are developed, i.e. as per atomic ratio Fe: Co: Cr: Ni: Mo: Si = 1: 1: 1: 1: 1: x (x = 0.5, 1.0, 1.5). Laser cladding (LC) is employed to fabricate the HEA coating on Q235 steel substrates as it can offer small heat-affected zone, lower dilution rate and good metallurgical bonding between coating and substrate [22-24]. The effect of Si addition in the new $FeCoCrNiMoSi_x$ system on its microstructure and thereafter tribological propterties and microhardness is systematically investigated.

2. Experimental

2.1 Materials preparation

Pre-alloyed $FeCoCrNiMoSi_x$ powders were prepared through a vacuum induction gas atomization (VIGA) process. The particle size distributions are shown in Figure 1. The theoretical mass/atomic percentages of elements in the powder are shown in Table 1. The chemical composition of the powder was detected using an inductively coupled

plasma atomic emission spectrometer (ICP-AES). $FeCoCrNiMoSi_x$ (x = 0.5, 1.0, 1.5) HEA coatings were fabricated by a laser cladding facility (LC, Raycus RFL-C6000X, Wuhan) on Q235 steel plates. High purity argon gas was fed through the coaxial nozzle to prevent oxidation during the cladding process. The LC parameters were set as follows: laser power (P = 1250, 1500, 1750, 2000, 2250 and 2500 W), powder feeding rate (S = 10, 15 and 20 g/min) and scan speed (v = 420, 480, 540, 600, 660 and 720 mm/min). Single track deposition of $FeCoCrNiMoSi_{0.5}$ was carried out to work out the optimal parameters by observing the microstructure of the coating material on the cross-sectional view. The specimens were ground, polished and etched by a Keller's reagent (H_2O: HNO_3: HCl: HF = 95:2.5:1.5:1) and observed under an optical microscope (OM, Leica Microsystems DM4500P). Under the optimal parameters (laser power, scan speed and powder feeding rate), the cladding experiments were performed with an overlap ratio of 25%, 50% and 75% respectively to figure out the optimal value. A scanning electron microscope (SEM, FEI Quanta 650 FEG) was used to observe the defects in the coating and interface. The optimal overlap ratio was determined when the minimal amount of defects were observed.
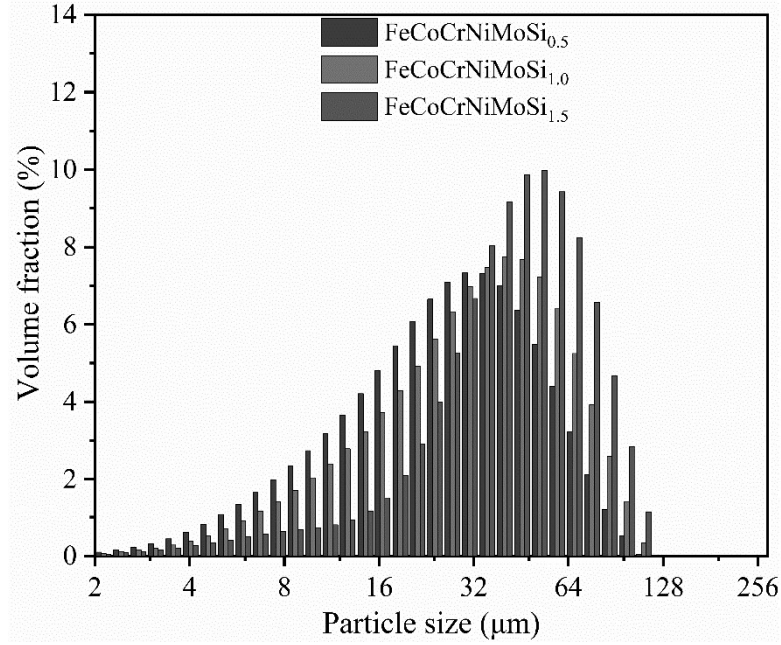
Figure 1. The particle size distribution.

Table 1.　The specific theoretical mass percentages of elements in powder.

(wt. %/ at. %)	Fe	Co	Cr	Ni	Mo	Si
FeCoCrNiMoSi$_{0.5}$	16.6/18.2	17.6/18.2	15.5/18.2	17.5/18.2	28.6/18.2	4.2/9.1
FeCoCrNiMoSi$_{1.0}$	16.0/16.7	16.9/16.7	14.9/16.7	16.8/16.7	27.5/16.7	8.0/16.7
FeCoCrNiMoSi$_{1.5}$	15.3/15.4	16.2/15.4	14.3/15.4	16.2/15.4	26.4/15.4	12.0/23.1

2.2 Microstructure

An X-ray diffractometer (XRD, Rigaku D/MAX-2250, Japan) was used to characterize the phase composition of the HEA cladding at a scanning voltage of 40 kV, a sweep current of 40 mA, a Cu Kα radiation source and a scan speed of 0.02 °/s. After grinding and polishing, a SEM equipped with a backscatter electron diffraction (BSED) analyzer (Oxford Instrument, UK) was used to characterize the microstructure of the HEA coatings. In addition, energy dispersive spectrometry (EDS) was performed to

reveal the distribution of elements in the HEA coatings.

2.3 Microhardness and tribological behaviors

An digital Vickers hardness tester (BUEHLER5104, America) was employed to measure the Vickers microhardness of the HEA coating at a load of 29.4 gf. Then, an HT-1000 pin-on-disc type high-temperature friction wear tester (ZhongkeKaihua Technology, Lanzhou, China) was used to investigate the coefficients of friction (COFs) of the $FeCoCrNiMoSi_x$ coatings under room temperature with a grinding material of Si_3N_4 ceramic ball, a load of 19.6 N, a friction speed of 0.5 m/s and a friction distance of 1050 m. Finally, the morphologies of wear debris and wear interfaces were observed by the SEM equipped with a BSED analyzer.

3. Results and discussion

3.1 Powder morphology and phase composition

The actual chemical compositions of the $FeCoCrNiMoSi_x$ (x = 0.5, 1.0, 1.5) powders are shown in Table 2, which are very close to the theoratical values. The morphology of the $FeCoCrNiMoSi_x$ (x = 0.5, 1.0, 1.5) powders are shown in Figure 2. The powders exhibit a good sphericity with some small satellite particles. With the increase of Si content, the amount of satellite particles on powder increases slightly, where small particles are prone to agglomerate.

Table 2. The actual chemical composition of the HEA powders (wt. %).

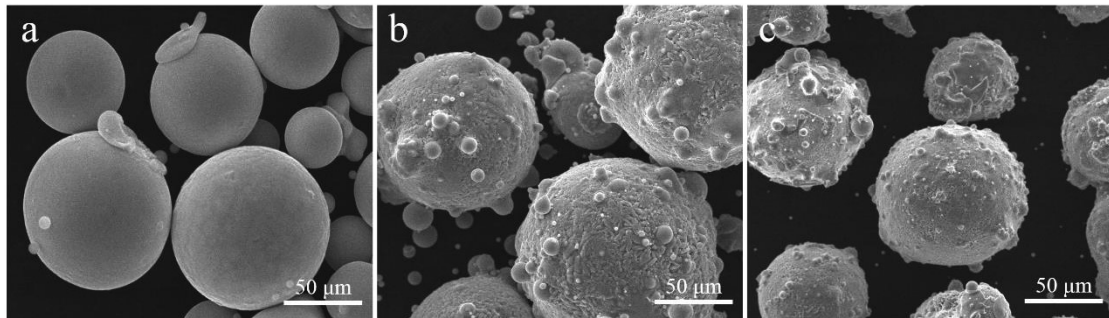|	Fe	Co	Cr	Ni	Mo	Si
FeCoCrNiMoSi$_{0.5}$	16.2	17.3	15.5	18.0	28.4	4.5
FeCoCrNiMoSi$_{1.0}$	15.6	16.5	14.8	17.1	27.4	8.5
FeCoCrNiMoSi$_{1.5}$	15.3	15.6	14.7	16.8	25.1	11.8

Figure 2. The morphologies of HEA powders prepared by gas atomization.

(a) FeCoCrNiMoSi$_{0.5}$ (b) FeCoCrNiMoSi$_{1.0}$ (c) FeCoCrNiMoSi$_{1.5}$

Figure 3 presents the XRD patterns of the powders. The HEA powders prepared by gas atomization mainly consist of Fe-rich FCC, FeMoSi phase and complex Si-rich intermetallics. The diffraction peak of FCC shifts to a higher angle with the increase of Si content. The addition of Si results in smaller lattice constant and lower diffraction intensity. The reduction of diffraction intensity among 43.5° can be attributed to the formation of FeMoSi phase, which consumes lots of iron and leads to a gradual decrease of Fe-rich FCC phase.
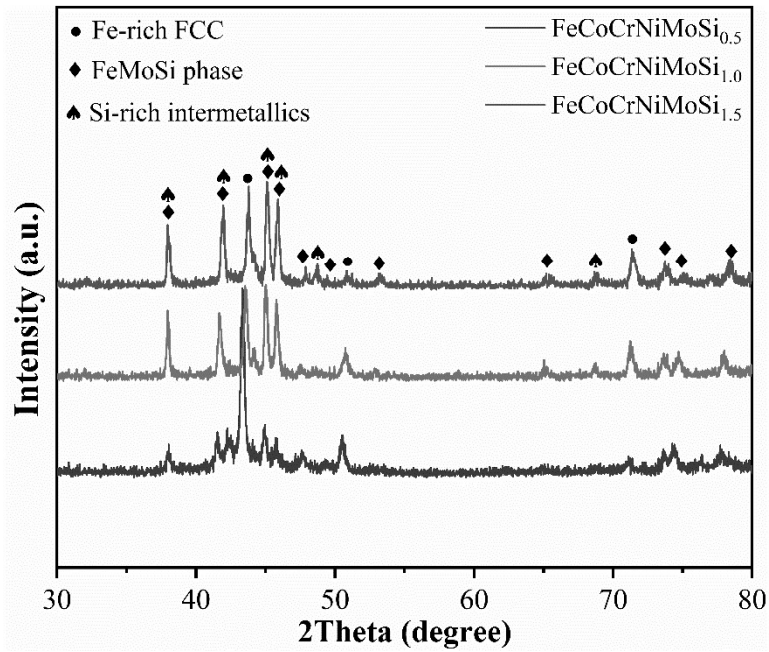
Figure 3. XRD spectrum of the HEA powders prepared by gas atomization.

3.2 Laser parameters and overlap ratio

During LC process, the operating parameters matters by controlling the microstructure and resulting properties [25]. Therefore, single track cladding tests of FeCoCrNiMoSi$_{0.5}$ with 108 combinations of laser power (P = 1250, 1500, 1750, 2000, 2250, 2500 W), powder feeding rate (S = 10, 15, 20 g/min), laser spot radius of 5 mm and scan speed (v = 420, 480, 540, 600, 660, 720 mm/min) were employed to obtain HEA coatings correspondingly (shown in Figure 4). In order to better explore the influence of process parameters on molten pool morphology, three groups of typical morphology were selected for observation in greater details, as shown in Figure 5. The morphologies of the molten pool and heat affect zone (HAZ) are marked in red dashed lines shown in Figure 5 e. With the increasing power, the molten pool region expands

to a larger size and the amount of gas pores first decrease and then increase (Figure 5 a-c). Low scan speed (Figure 5 d) results in more gas pores with small size, while high scan speed (Figure 5 f) leads to larger size of gas pores and lack of fusions. Moreover, with the increase of powder feeding rate, the color of molten pool tends to be darker (shown in Figure 5 j), which demonstrates an insufficient metallurgical combination between substrate and coatings. The coating under the 10 g/s powder feeding rate has a larger molten pool. However, the coating seems too little to be fabricated in a reasonable time (Figure 5 h). Based on the criteria of controlled defect numbers and good metallurgical combination in cross-sectional view of the molten pool region, the optimized LC coating techniques were fixed at P = 2250 W, S = 15 g/s, and v = 480 mm/min during the following fabrication processes.
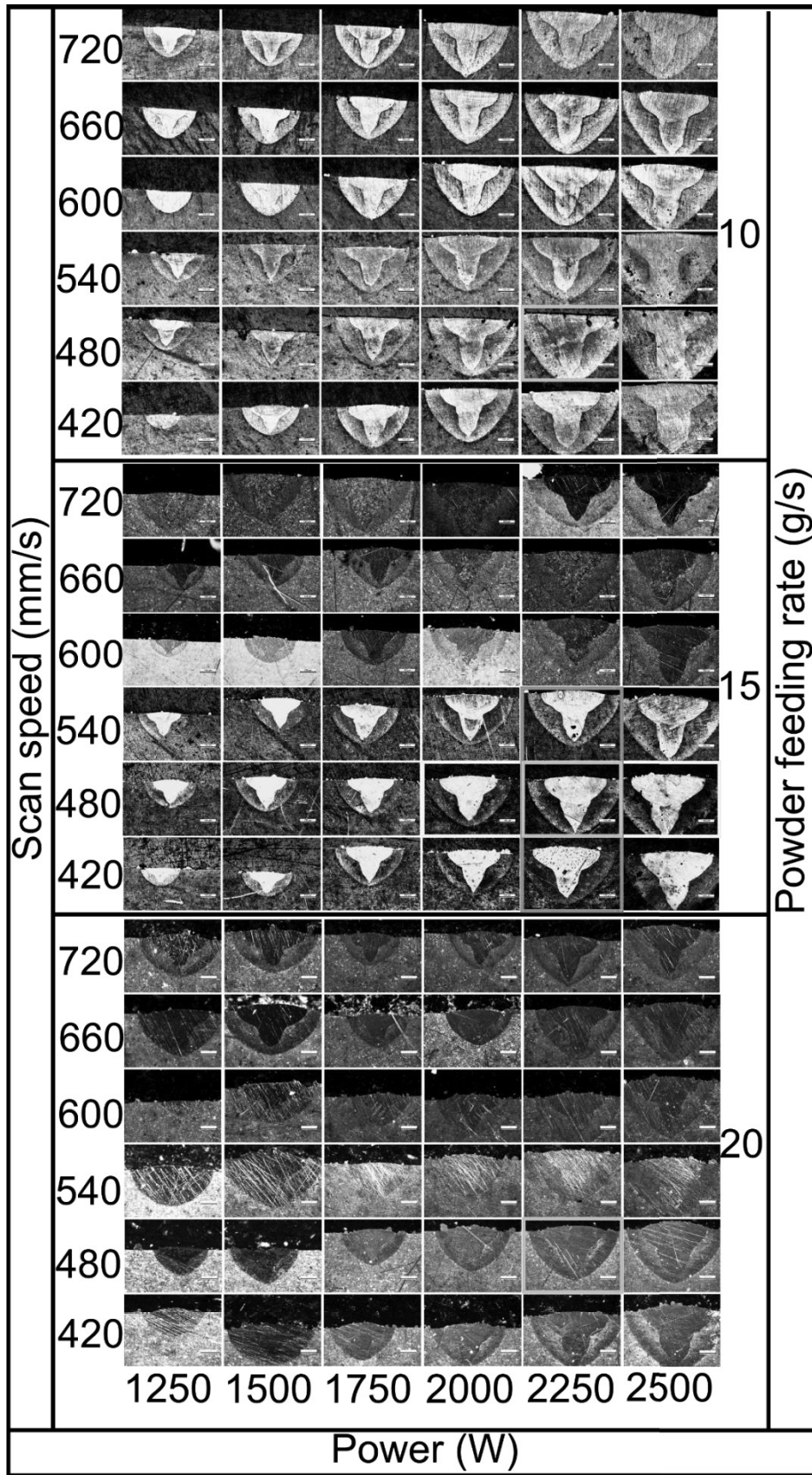
Figure 4. The cross sectional views of molten pool region obtained through different
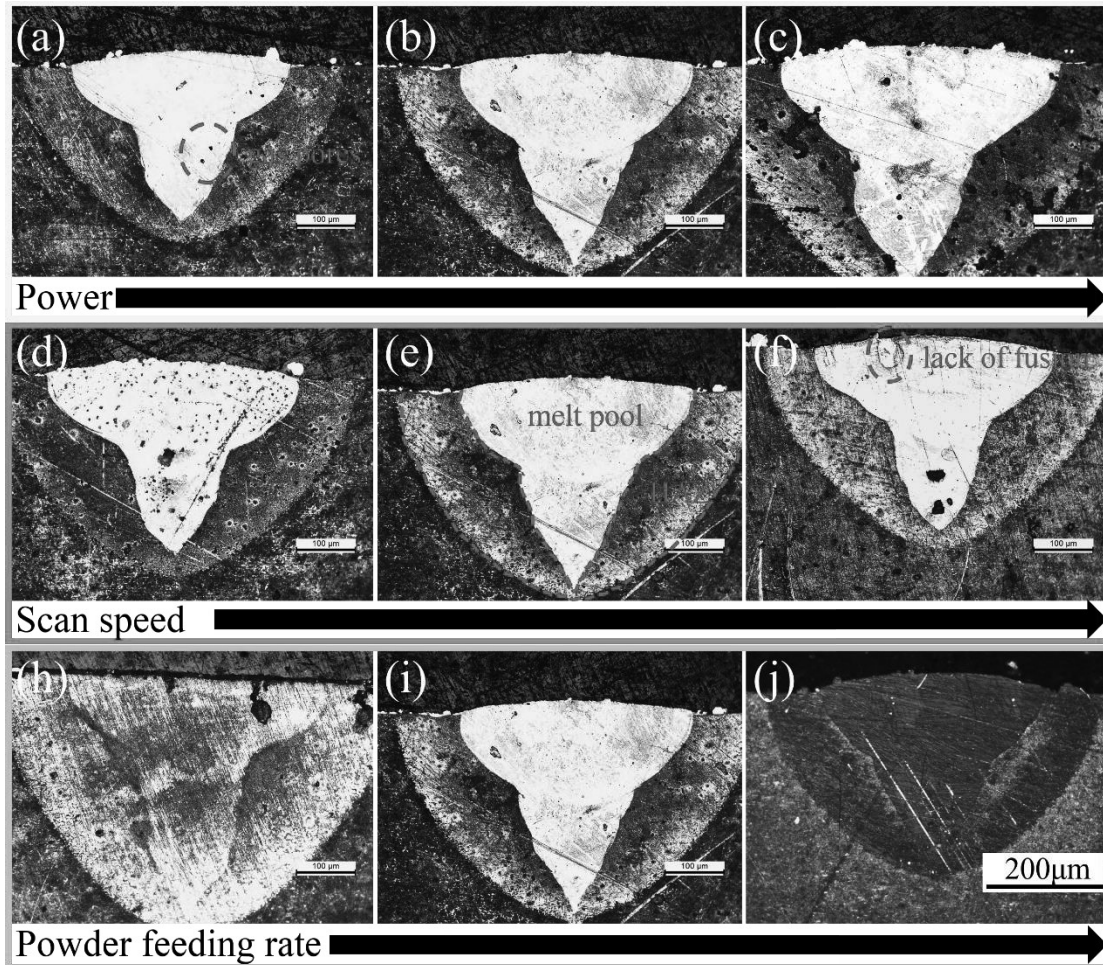
processing parameters.

Figure 5. The typical cross-sectional morphology of molten pool region, a-c: 2000, 2250 and 2500 W (marked in yellow box in Figure 4); d-f: 420, 480 and 520 mm/min (marked in blue box in Figure 4); h-j: 10, 15 and 20 g/s (marked in orange box in Figure 4).

Three groups of overlap experiment were carried out with the above-mentioned laser process parameters to obtain the optimal combination between the LC coating and the substrate. The overlap ratios were tested at 25%, 50%, and 75% respectively and the corresponding cross-sectional morphologies of LC HEA coatings are shown in Figure 6. Pores exist in all three HEA coatings. However, the lack of fusion and cracks

only exist in the $FeCoCrNiMoSi_{0.5}$ and $FeCoCrNiMoSi_{1.5}$ coating respectively. As the overlap ratio increases, the lack of fusion disappears and the number of pores first decrease and then increase. The interface between the coatings and substrates (yellow dashed line in Figure 6) is more smooth in $FeCoCrNiMoSi_{1.0}$. The 50% overlap ratio was selected as the optimal value as the pores were less and smaller in size. Therefore, final LC optimal parameters were obtained as P = 2250 W, S = 15 g/min, v = 480 mm/min and 50% overlap ratio.
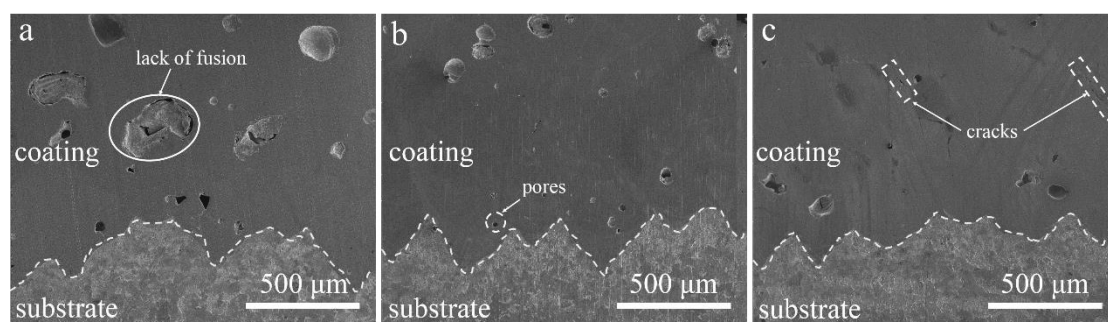

Figure 6. The cross-sectional morphologies of the coating obtained from three over lap ratios: (a) 25%, (b) 50%, (c) 75%.

3.3 Microstructure

Based on the XRD pattern shown in Figure 7, three LC HEA coatings are mainly composed of Fe-rich FCC phase, FeMoSi phase and Si-rich intermetallics. The addition of Si in FeCoCrNiMo HEA system facilitates the formation of Si-rich intermetallics, whose formation is related to the more negative mixing enthalpy ($\leq$ -20 kJ/mol) between Si and other elements as shown in Table 3. The phase composition was

calculated using Jade 6 and shown in Table 4. The XRD peak of FeMoSi phase decreases with the increase of Si content. In addition, it could be found that the diffraction peaks at high angles (65-80°) are relatively weak in the XRD diffraction pattern. The different size of elemental atoms results in significant distortion in crystal lattice. Therefore, as the diffraction angle becomes larger, the resulting diffuse scattering is enhanced, making the intensity of the diffraction peak weaker [26].

Table 3. The mixing enthalpy (ΔH_{mix}/kJ·mol^{-1}) among different elements of FeCoCrNiMoSi HEA system [27].

ΔH_{mix}/kJ·mol^{-1}	Fe	Co	Cr	Ni	Mo	Si
Fe	\	-1	-1	-2	-2	-35
Co	\	\	-4	0	-5	-38
Cr	\	\	\	-7	0	-37
Ni	\	\	\	\	-7	-40
Mo	\	\	\	\	\	-35

Table 4. The phase composition calculated by Jade 6.

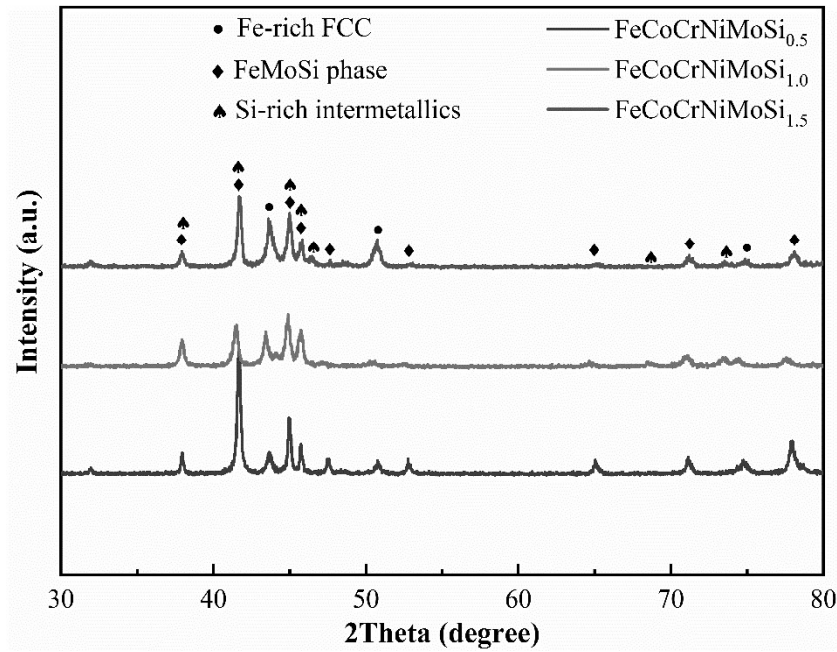| (%)	Fe-rich FCC phase	FeMoSi phase	Si-rich intermetallics
FeCoCrNiMoSi$_{0.5}$	15.0	85.0	0
FeCoCrNiMoSi$_{1.0}$	17.3	80.2	2.5
FeCoCrNiMoSi$_{1.5}$	30.6	63.6	5.8

Figure 7. The XRD of LC FeCoCrNiMoSi HEA coatings.

Figure 8 shows the microstructure and element distribution of the LC HEA coatings. The EDS results indicate that the bright phase is rich in Mo and Si, while the dark phase is rich in Fe, Cr and Ni. Combined with the XRD analysis, it can be concluded that the bright phase mainly consists of the FeMoSi phase and the dark phase is the Fe-FCC phase. Further observation finds that the FeMoSi phase has alternating elliptic and dendritic morphologies. The FeMoSi phase obtained in the first cladding layer expressed equiaxed grain owing to the high cooling rate and large degree of supercooling in LC process [28]. When the second layer was deposited, the previous layer was partially remelted and the decreased degree of supercooling was insufficient to maintain the high driving force of nucleation. Therefore, the constitutional supercooling became dominant, leading to a dendritic morphology of FeMoSi phase. In Figure 8 a, b and c, strong metallurgical bond were formed between the HEA coatings

and the substrates. The bottom of the cladding layer that adjcent to the substrate has a narrow planar crystallization zone, which is featured as "white bright band" in SEM [29]. The existence of the "white bright band" may relate to the solidification process. The rapid solidification process induces a super high cooling rate on the surface of the matrix, which leads to the growth of planar crystals in this area. In addition, as the proportion of Si elevates, the "white bright band" becomes narrower. This might be attributed to the enhancement of the shrinkage rate caused by the excessive Si content. The addition of silicon leads to a tighter shrinkage during the planar crystal solidification process [30]. Figure 8 d, e, and f are the microstructures in an area extended to the region highlighted with black dash box in Figure 8 a,b and c. The EDS analysis found that the content of Fe in the coating was higher than the theoretical value because of the Q235 steel substrate was remelted and mixed into the molten pool during the LC process, where a proportion of Fe element was finally retained in the HEA coatings.

Element	At%
SiK	16.91
MoL	22.30
CrK	12.64
FeK	22.64
CoK	14.30
NiK	11.21

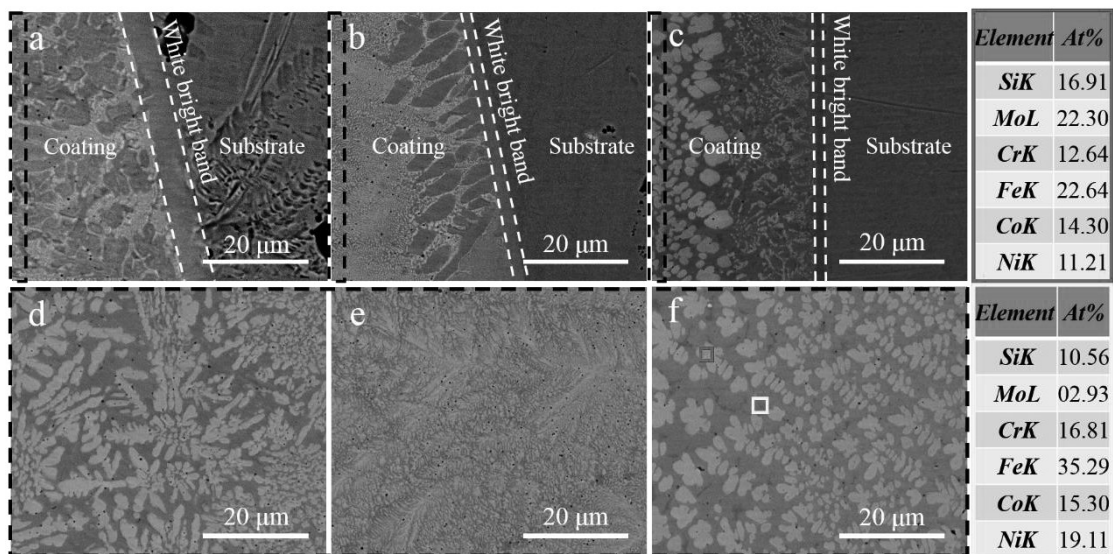| Element	At%
SiK	10.56
MoL	02.93
CrK	16.81
FeK	35.29
CoK	15.30
NiK	19.11

Figure 8. The microstructure and element distribution of LC HEA coatings in longitudinal direction. a, b and c are the microstructures of the longitudinal plane between HEA coatings and matrix $FeCoCrNiMoSi_x$ (x = 0.5, 1.0, 1.5), respectively. d, e and f are the microstructures in an extended area (in black dashed box) of the $FeCoCrNiMoSi_x$ (x = 0.5, 1.0, 1.5) coatings, respectively.

3.4 Tribological behaviors and microhardness

Figure 9 presents the coefficients of friction (COFs) of the $FeCoCrNiMoSi_x$ (x = 0.5, 1.0, 1.5) HEA coatings. The relatively smooth curves of COFs may be related to the fine microstructure from high cooling rate during LC process. The average COFs of three LC HEA coatings are 0.360, 0.375 and 0.333, respectively.
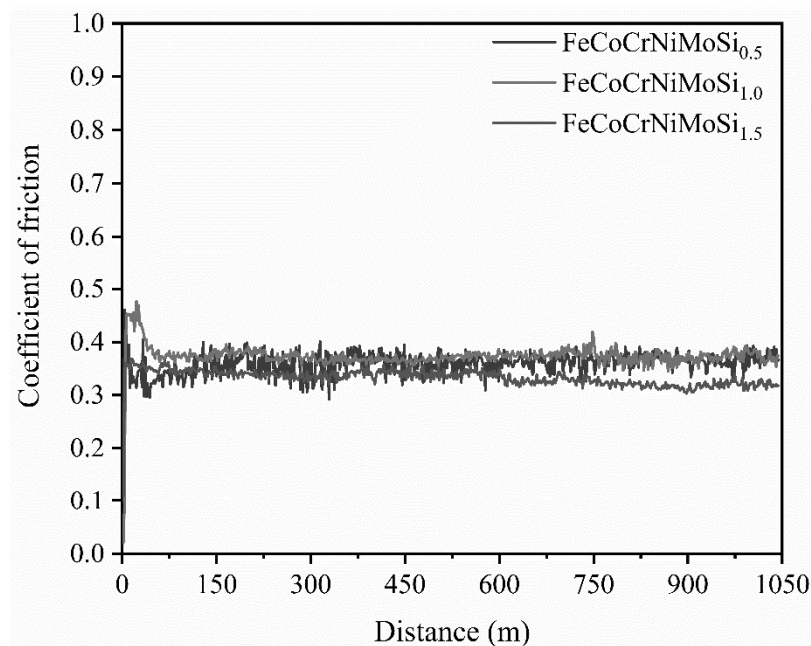

Figure 9. The COFs of LC $FeCoCrNiMoSi_x$ (x = 0.5, 1.0, 1.5) coatings in 1050 m.

Figure 10 shows the microhardness and wear rate during friction and wear process of the as-cast $FeCoCrNiMo_{0.3}$ HEA [17] and LC $FeCoCrNiMoSi_x$ HEA coatings. The hardness increased with the increasing amount of intermetallics [31]. The wear rate was calculated based on Archard's law [32]:

$$R = V_{loss}/N \cdot S \qquad (1)$$

where R is the wear rate ($mm^3 \cdot N^{-1} \cdot m^{-1}$), V_{loss} is the volumetric loss (mm^3), which can be obtained from M_{loss}/ρ (where M_{loss} is the wear mass loss during the wear test and ρ is the density of three samples), N represents the applied load (N) and S represents the total sliding distance (m).

As obviously shown in Figure 10, the hardness has seen a large improvement and the wear rate reduces compared with the as-cast $FeCoCrNiMo_{0.3}$ HEA [17]. When the Si content is increased from 0.5 to 1.0, the hardness of the LC coating increases from 784 to 826 HV with the wear rate reducing from 0.137 to 0.107 $\times 10^{-4}$ $mm^3 \cdot N^{-1}m^{-1}$. This indicates an enhanced wear resistance and conforms the Archard's law [32, 33] (which defines that the wear rate is inversely proportional to hardness and is mainly based on single wear mechanism). When the Si content further increases from 1.0 to 1.5, the hardness of the coating increases from 826 to 943 HV and the wear rate increases from 0.107 to 0.753 $\times 10^{-4}$ $mm^3 \cdot N^{-1}m^{-1}$ during friction process, which does not obey the Archard's law anymore. This phenomenon is unique in the $FeCoCrNiMoSi_x$ HEA coating materials and need to be investigated in further details.
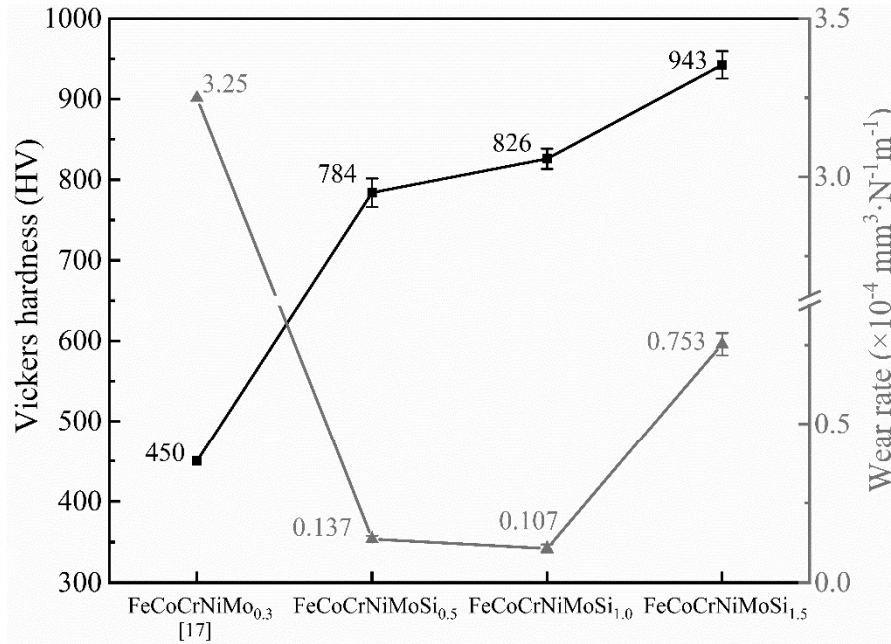
Figure 10. The Vickers hardness and wear rate in friction and wear process of the LC

HEA coatings compared with $FeCoCrNiMo_{0.3}$ [17].

As shown in Figure 11 a and b, the wear interfaces of $FeCoCrNiMoSi_{0.5}$ and

$FeCoCrNiMoSi_{1.0}$ HEA coatings have uniform and parallel scratches with some micro-

particles on the friction interface. In addition, small adhesion part and plastic

deformation are obvious in Figure 11 a and b, which is a characteristic of adhesive wear

[34, 35]. In Figure 11 c, large delamination exists at the $FeCoCrNiMoSi_{1.5}$ wear

interface. The wear debris of $Si_{0.5}$ and $Si_{1.0}$ HEA coatings have relatively smaller sizes

(except for some large fragmentation in Figure 11 a and e).

The morphology of longitudinal section in Figure 12 a-b proves that deformation

layers exist in the wear surface of $FeCoCrNiMoSi_{0.5}$ and $FeCoCrNiMoSi_{1.0}$ HEA

coatings. While there is an obvious crack existing in the wear surface of

$FeCoCrNiMoSi_{1.5}$ coatings (shown in Figure 12 c). Combined with the morphology and

wear debris, the main wear mechanism of the $FeCoCrNiMoSi_{0.5}$ and $FeCoCrNiMoSi_{1.0}$ HEA coatings are combined abrasive and adhesive wear [34, 36]. However, the proportion of abrasive wear in $FeCoCrNiMoSi_{1.0}$ HEA coatings is higher than that of $FeCoCrNiMoSi_{0.5}$ HEA coatings due to the amount of smaller size debris and the morphology of the interface as confirmed from Figure 11 a, b and f. For the $FeCoCrNiMoSi_{1.5}$ HEA coating, larger wear rate was observed, as illustrated in Figure 10. Due to the cracks and other defects formed by increasing shrinkage rate, large pieces of materials were peeled off from the defects site during friction process. These large peeled layers after shedding are crushed again to form the morphology of broken delamination as shown in Figure 11 c. Moreover, the size of debris in Figure 11 g is much larger than the paralleled samples. This is a typical feature of delamination wear [37-39]. The intermetallic compounds as a function of harder and more brittle phases, can damage the plastic of the sample. The increasing solid solution strengthening and the formation of intermetallics induced by Si raised the hardness of the HEAs coatings while increased the brittleness of HEA coatings [40]. At the same time, the shrinkage of the HEA coating during the rapid cooling process is too large compared with the Q235 matrix, and penetration cracks are generated during the solidification process. During the friction and wear process, the strong friction vibration made the coating fragmentation occur at the friction interface, resulting in a large number of peeling layer and a sudden increment in the wear rate of $FeCoCrNiMoSi_{1.5}$.
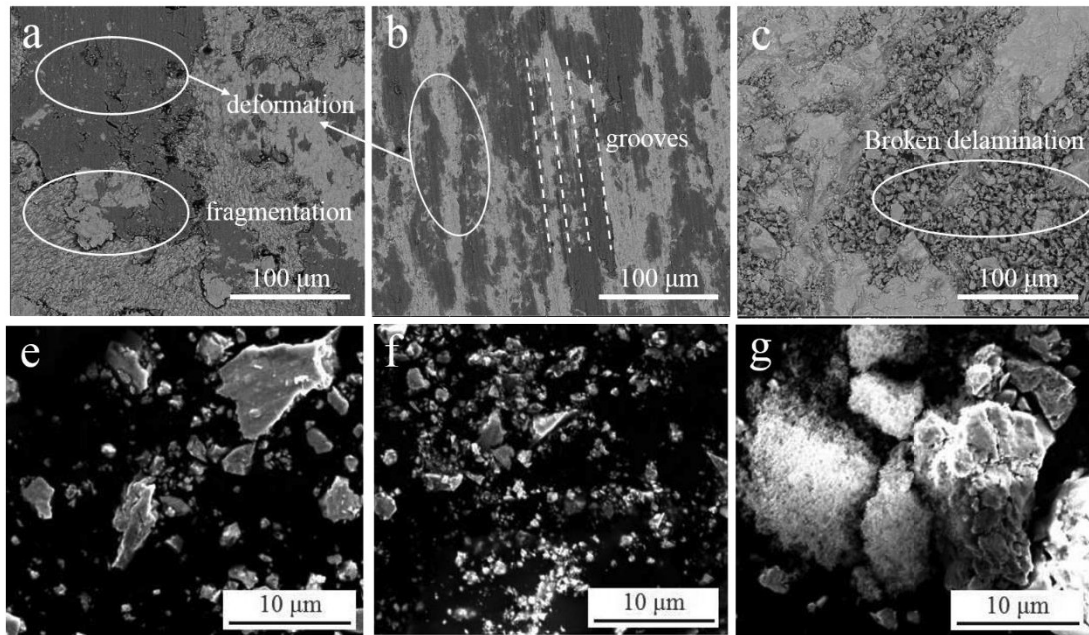
Figure 11. a-c: The backscattered electron images of wear interface morphology of FeCoCrNiMoSi$_{0.5}$, FeCoCrNiMoSi$_{1.0}$ and FeCoCrNiMoSi$_{1.5}$ coatings, respectively, e-g: the secondary electron images of the wear debris of FeCoCrNiMoSi$_{0.5}$, FeCoCrNiMoSi$_{1.0}$ and FeCoCrNiMoSi$_{1.5}$ coatings, respectively.
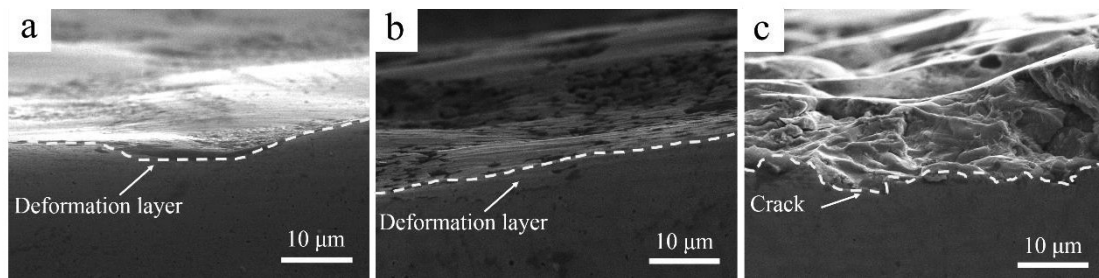

Figure 12. The morphology of longitudinal section of wear surface.

(a) FeCoCrNiMoSi$_{0.5}$ (b) FeCoCrNiMoSi$_{1.0}$ (c) FeCoCrNiMoSi$_{1.5}$

The EDS analyses of the oxygen ratio in the dark area and wear debris of FeCoCrNiMoSi$_{1.0}$ are shown in Figure 13. It can be found that with the increase of Si molar ratio, the oxygen content of HEA coating wear debris initially increases and then

decreases. When the Si content ratios are 0.5 and 1.0, the oxygen content on the friction interface changes in the same trend as that of the wear debris. The main reason for the abnormal oxide content of $FeCoCrNiMoSi_{1.5}$ is the shorter contacting time. The friction interaction of $FeCoCrNiMoSi_{1.5}$ coating is short due to a tendency of fragmentation, which is unable to generate enough heat to facilitate severe oxidation. Therefore, the oxygen content of the obtained wear debris stays at a relatively lower level. The $FeCoCrNiMoSi_{1.0}$ HEA coating is easier to be oxidized due to a larger amount of scratches and the smaller size of debris which increases the area exposed to the atomsphere (shown in Figure 11, e). However, the $FeCoCrNiMoSi_{1.0}$ HEA coating has more oxide layer to delay the friction process. This could lead to an increase of the COFs and a reduction of wear rate and finally improve the wear resistance of $FeCoCrNiMoSi_{1.0}$ HEA coating.
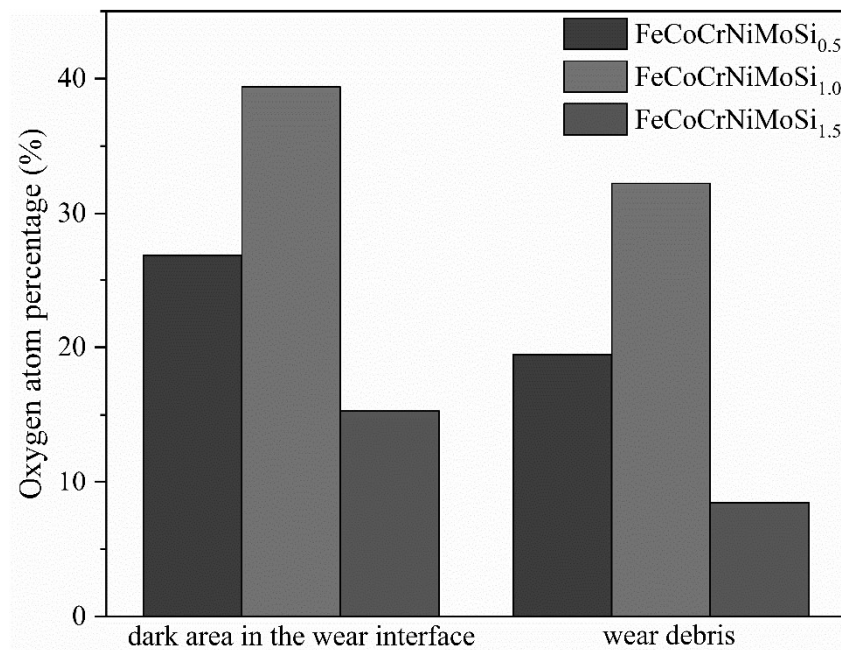

Figure 13. The EDS analysis of the oxygen ratio in the dark area wear interface and

wear debris.

4. Conclusions

In summary, FeCoCrNiMoSi$_x$ (x = 0.5, 1.0, 1.5) HEA coatings were successfully fabricated on the Q235 steel substrate by laser cladding. The coatings consist of considerably amount of defects, including porosities, cracks and lack of fusion, due to the large cooling rate. The microstructure of the coating materials mainly consist of Fe-rich FCC and FeMoSi phases, where the Si addition induced severe distortion in crystal lattice. Compared with the original as-casted FeCoCrNiMo HEA, the FeCoCrNiMoSi$_x$ coatings generally offers significantly larger micro-hardness and smaller coefficient of frictions and wear rate. The FeCoCrNiMoSi$_{1.0}$ HEA coating exhibits the highest wear resistance. The wear mechanism for HEA coatings with Si addition up to 1.0 is mainly a combined abrasive and adhesive wear. When the Si content increases to 1.5, although the hardness further increases, the coating tends to partially broke during friction test indicating a delimination wear mechanism, which therefore worsen the wear resistance.

CrediT authorship contribution statement

Yucheng Yang: Conceptualization, Data curation, Methodology, Writing - original draft. **Yaojia Ren:** Conceptualization, Formal analysis, Investigation, Methodology. **Yanwen Tian:** Conceptualization. **Kaiyang Li:** Conceptualization, writing - review & editing. **Lichun Bai:** Conceptualization. **Qianli Huang:** Conceptualization, Methodology. **Quan Shan:** Conceptualization, Methodology. **Yingtao Tian:** Conceptualization, Methodology g. **Hong Wu:** Funding acquisition, Writing - review & editing.

Declaration of Competing Interest

The authors declared that they do not have any commercial or associative interest that represents conflicts of interest in connection with the work submitted.

Acknowledgements

Reference

[1] M. Dong, T. Hao, Z. Yong, L. Yi, Correlation between glass formation and type of eutectic coupled zone in eutectic alloys, Materials Transactions 44(10) (2003) 2007-2010.

[2] A. Fu, W. Guo, B. Liu, Y. Cao, L. Xu, Q. Fang, H. Yang, Y. Liu, A particle reinforced NbTaTiV refractory high entropy alloy based composite with attractive mechanical properties, Journal of Alloys and Compounds 815 (2020) 152466.

[3] W. Li, X. Long, S. Huang, Q. Fang, C. Jiang, Elevated fatigue crack growth resistance of Mo alloyed CoCrFeNi high entropy alloys, Engineering Fracture Mechanics 218 (2019) 106579.

[4] B. Cantor, I.T.H. Chang, P. Knight, A.J.B. Vincent, Microstructural development in equiatomic multicomponent alloys, Materials Science and Engineering A 375 (2004) 213-218.

[5] J.W. Yeh, S.K. Chen, S.J. Lin, J.Y. Gan, T.S. Chin, T.T. Shun, C.H. Tsau, S.Y. Chang, Nanostructured high-entropy alloys with multiple principal elements: Novel alloy design concepts and outcomes, Advanced Engineering Materials 6(5) (2004) 299-303.

[6] J. Peng, F. Li, B. Liu, Y. Liu, P.K. Liaw, Mechanical properties and deformation behavior of a refractory multiprincipal element alloy under cycle loading, Journal of Micromechanics and Molecular Physics 05(04) (2021) 2050014.

[7] Y.J. Zhao, J.W. Qiao, S.G. Ma, M.C. Gao, H.J. Yang, M.W. Chen, Y. Zhang, A hexagonal close-packed high-entropy alloy: The effect of entropy, Materials & Design 96 (2016) 10-15.

[8] J.W. Yeh, S.K. Chen, J.Y. Gan, S.J. Lin, T.S. Chin, T.T. Shun, C.H. Tsau, S.Y. Chang, Formation of simple crystal structures in Cu-Co-Ni-Cr-Al-Fe-Ti-V alloys with multiprincipal metallic elements, Metallurgical and Materials Transactions A-Physical Metallurgy and Materials Science 35A(8) (2004) 2533-2536.

[9] L. Jia, Q. Fang, B. Liu, Y. Liu, Y. Liu, Atomic-scale analysis of nanoindentation behavior of high-entropy alloy, Journal of Micromechanics and Molecular Physics 01(01) (2016) 1650001.

[10] M. Zhang, X. Zhou, X. Yu, J. Li, Synthesis and characterization of refractory TiZrNbWMo high-entropy alloy coating by laser cladding, Surface & Coatings Technology 311 (2017) 321-329.

[11] H.L. Wang, Q.B. Liu, Y.X. Guo, H.W. Lan, MoFe1.5CrTiWAlNbx refractory high-entropy alloy coating fabricated by laser cladding, Intermetallics 115 (2019) 106613.

[12] Z.B. Cai, X.F. Cui, Z. Liu, Y. Li, M.L. Dong, G. Jin, Microstructure and wear resistance of laser cladded Ni-Cr-Co-Ti-V high-entropy alloy coating after laser remelting processing, Optics and Laser Technology 99 (2018) 276-281.

[13] C. Dai, T. Zhao, C. Du, Z. Liu, D. Zhang, Effect of molybdenum content on the microstructure and corrosion behavior of FeCoCrNiMox high-entropy alloys, Journal of Materials Science & Technology 46 (2020) 64-73.

[14] T. Fujieda, H. Shiratori, K. Kuwabara, M. Hirota, T. Kato, K. Yamanaka, Y. Koizumi, A. Chiba, S. Watanabe, CoCrFeNiTi-based high-entropy alloy with superior tensile strength and corrosion resistance achieved by a combination of additive manufacturing using selective electron beam melting and solution treatment, Materials Letters 189 (2017) 148-151.

[15] R. Zhou, Y. Liu, C. Zhou, S. Li, W. Wu, M. Song, B. Liu, X. Liang, P.K. Liaw, Microstructures and mechanical properties of C-containing FeCoCrNi high-entropy alloy fabricated by selective laser melting, Intermetallics 94 (2018) 165-171.

[16] Y. Geng, J. Chen, H. Tan, J. Cheng, J. Yang, W. Liu, Vacuum tribological behaviors of CoCrFeNi high entropy alloy at elevated temperatures, Wear 456-457 (2020) 203368.

[17] G. Deng, A.K. Tieu, L. Su, P. Wang, L. Wang, X. Lan, S. Cui, H. Zhu, Investigation into reciprocating dry sliding friction and wear properties of bulk CoCrFeNiMo high entropy alloys fabricated by spark plasma sintering and subsequent cold rolling processes: Role of Mo element concentration, Wear 460-461 (2020) 203440.

[18] H. Fan, Y. Liu, S. Yang, Martensite decomposition during post-heat treatments and the aging response of near-α Ti–6Al–2Sn–4Zr–2Mo (Ti-6242) titanium alloy processed by selective laser melting (SLM), Journal of Micromechanics and Molecular Physics (2021) 2050018.

[19] A. Kumar, P. Dhekne, A.K. Swarnakar, M.K. Chopkar, Analysis of Si addition on phase formation in AlCoCrCuFeNiSix high entropy alloys, Materials Letters 188 (2017) 73-76.

[20] R. Babilas, W. Lonski, P. Borylo, M. Kadziolka-Gawel, P. Gebara, A. Radon, The influence of cooling rate, chromium and silicon addition on the structure and properties of AlCoCrFeNiSi high entropy alloys, Journal of Magnetism and Magnetic Materials 502 (2020) 166492.

[21] B. Gorr, F. Mueller, H.J. Christ, T. Mueller, H. Chen, A. Kauffmann, M. Heilmaier, High temperature oxidation behavior of an equimolar refractory metal-based alloy 20Nb-20Mo-20Cr-20Ti-20Al with and without Si addition, Journal of Alloys and Compounds 688 (2016) 468-477.

[22] J. Liu, E. Stevens, Q. Yang, M. Chmielus, A.C. To, An analytical model of the melt pool and single track in coaxial laser direct metal deposition (LDMD) additive manufacturing, Journal of Micromechanics and Molecular Physics 02(04) (2018) 1750013.

[23] Y. Han, L. Wang, K. Liu, W. Yan, Numerical modeling of laser powder bed fusion of metallic glasses: Prediction of crystallization, Journal of Micromechanics and Molecular Physics 05(04) (2021) 2050013.

[24] C. Yan, G. Ma, A. Chen, Y. Chen, J. Wu, W. Wang, S. Yang, Y. Shi, Additive manufacturing of hydroxyapatite and its composite materials: A review, Journal of Micromechanics and Molecular Physics 05(03) (2021) 2030002.

[25] H. Wu, J. Ren, Q. Huang, X. Zai, R. Li, Effect of laser parameters on microstructure, metallurgical defects and property of AlSi10Mg printed by selective laser melting, Journal of Micromechanics and Molecular Physics 02(4) (2017) 1750017.

[26] C.J. Tong, Y.L. Chen, S.K. Chen, J.W. Yeh, T.T. Shun, C.H. Tsau, S.J. Lin, S.Y. Chang, Microstructure characterization of AlxCoCrCuFeNi high-entropy alloy system with multiprincipal elements, Metallurgical and Materials Transactions A-Physical Metallurgy and Materials Science 36A(4) (2005) 881-893.

[27] A. Takeuchi, A. Inoue, Calculations of Mixing Enthalpy and Mismatch Entropy for Ternary Amorphous Alloys, Materials Transactions JIM 41(11) (2000) 1372-1378.

[28] L. Ai, X.L. Gao, Micromechanical modeling of 3D printable interpenetrating phase composites with tailorable effective elastic properties including negative Poisson's ratio, Journal of Micromechanics and Molecular Physics 02(4) (2018) 1750015.

[29] M.X. Li, Y.Z. He, G.X. Sun, Laser cladding Co-based alloy/SiCp composite coatings on IF steel, Materials & Design 25(4) (2004) 355-358.

[30] C.M. Liu, H.M. Wang, S.Q. Zhang, H.B. Tang, A.L. Zhang, Microstructure and oxidation behavior of new refractory high entropy alloys, Journal of Alloys and Compounds 583 (2014) 162-169.

[31] C. Zheng, Q. Liu, S. Zheng, X. Chong, Y. Jiang, J. Feng, Effect of solution treatment on mechanical properties and microstructure of welded joints of Fe-29Mn-9Al-0.9C low-density steel, Journal of Micromechanics and Molecular Physics 05(02) (2020) 2050006.

[32] J.F. Archard, Contact and Rubbing of Flat Surfaces, Journal of Applied Physics 24(8) (1953) 981-988.

[33] H. Chen, G. Zhang, Z. Lu, X. Li, N. Srikanth, L. Bai, Tribological behaviors of DLC films with hierarchical surface textures under water lubrication: A molecular dynamic simulation, Journal of Micromechanics and Molecular Physics (2021) 2150005.

[34] Stachowiak, W. Gwidon, Engineering Tribology (Third Edition), 2006.

[35] C. Xiang, Y. Liu, B. Liu, Y. Ca O, Z. Gan, Characterization of hot deformation behavior of Ti–3Al–5Mo–4.5V alloy with a martensitic starting microstructure, Journal of Micromechanics and Molecular Physics 02(03) (2017) 1750011.

[36] G.W. Stachowiak, A.W. Batchelor, Engineering Tribology (Third Edition), 2006.

[37] N.P. Suh, An overview of the delamination theory of wear, Wear 44(1) (1977) 1-16.

[38] H. Wu, Y. Ren, J. Ren, A. Cai, M. Song, Y. Liu, X. Wu, Q. Li, W. Huang, X. Wang, I. Baker, Effect of melting modes on microstructure and tribological properties of selective laser melted AlSi10Mg alloy, Virtual and Physical Prototyping 15 (2020) 570-582.

[39] Y. Ren, L. Liang, Q. Shan, A. Cai, J. Du, Q. Huang, S. Liu, X. Yang, Y. Tian, H. Wu, Effect of volumetric energy density on microstructure and tribological properties of FeCoNiCuAl high-entropy alloy produced by laser powder bed fusion, Virtual and Physical Prototyping 15 (2020) 543-554.

[40] V. Dolique, A.L. Thomann, P. Brault, Y. Tessier, P. Gillon, Complex structure/composition relationship in thin films of AlCoCrCuFeNi high entropy alloy, Materials Chemistry And Physics 117(1) (2009) 142-147.